Taylor & Francis
Taylor & Francis Group

Phase Transitions
A Multinational Journal

ISSN: 0141-1594 (Print) 1029-0338 (Online) Journal homepage: www.tandfonline.com/journals/gpht20

Structural, microstructural and electrical properties of PB–ZTS ternary ceramics

Kahoul Fares, Tabchouche Ahmed, Chebli Derradji, Bouguettoucha Abdallah & Dizge Nadir

To cite this article: Kahoul Fares, Tabchouche Ahmed, Chebli Derradji, Bouguettoucha Abdallah & Dizge Nadir (2025) Structural, microstructural and electrical properties of PB–ZTS ternary ceramics, Phase Transitions, 98:8, 534-544, DOI: 10.1080/01411594.2025.2553134

To link to this article: https://doi.org/10.1080/01411594.2025.2553134

Published online: 16 Sep 2025.

PHASE TRANSITIONS
2025, VOL. 98, NO. 8, 534–544
https://doi.org/10.1080/01411594.2025.2553134

Taylor & Francis
Taylor & Francis Group

Structural, microstructural and electrical properties of PB–ZTS ternary ceramics

Kahoul Fares[a,b], Tabchouche Ahmed[c], Chebli Derradji[d], Bouguettoucha Abdallah[d] and Dizge Nadir[e]

[a]Département Socle Commun ST, Faculté de Technologie, Université de M'Sila, M'Sila, Algérie; [b]Département de Chimie, Laboratoire de Chimie Appliquée, Université de Biskra, RB-Biskra, Algérie; [c]Département Génie des Procédés, Laboratoire de Dynamique, Interaction et Réactivité des Systèmes, Université de Ouargla, Ouargla, Algérie; [d]Department of Engineering Process, Faculty of Technology, Ferhat ABBAS University Setif, Setif, Algeria; [e]Department of Environmental Engineering, Mersin University, Mersin, Turkey

ABSTRACT

The solid solution of $Pb_{0.92}Ba_{0.08}(Zr_{0.49}Ti_{0.51})_{1-x}Sn_xO_3$ (PB–ZTS) ceramics with x = 0, 0.02, 0.04 and 0.06 was prepared via the traditional solid-state reaction method. Further, the effect of excessive Sn substitution at Zr/Ti-site on structural, morphological, dielectric and piezoelectric properties was studied. X-ray diffraction (XRD) analysis confirmed that all samples crystallized into a combination of perovskite and pyrochlore phases. The morphotropic phase boundary (MPB) of the ternary system, located between the rhombohedral and tetragonal phases, is observed at around x = 0.04. The Raman-active modes of PB–ZTS were distinguished and assigned based on group theory analysis. Scanning electron microscopy (SEM) analysis reveals microstructural variations, with the highest density and largest grain size observed at a Sn content of x = 0.04. The $Pb_{0.92}Ba_{0.08}(Zr_{0.49}Ti_{0.51})_{0.96}Sn_{O.04}O_3$ ceramic samples exhibit well-developed grains with an average size of 760.281 nm and demonstrate optimal properties: d_{33} = 465 pC/N, Kp = 0.604, Qm = 411, ε_r = 1654, tanδ = 3.293%, and a bulk density of 7.91 g/cm^3.

ARTICLE HISTORY
Received 18 June 2025
Accepted 22 August 2025

KEYWORDS
Ceramics; piezoelectric properties; PZT; Raman spectroscopy; XRD; MPB

1. Introduction

The perovskite structure, represented as ABO_3 (where A and B are cation sites with different valences, and O is the oxygen anion site), is one of the most versatile crystal structures, offering a wide range of applications in ceramic science and technology. Ferroelectric materials with a perovskite structure find extensive applications in electronic devices, including pyroelectric detectors, imaging systems, optical memories, deflectors, and modulators [1–3]. Lead zirconate titanate (PZT), with the chemical formula $Pb(Zr_{(1-x)}Ti_x)O_3$, is among the most advanced perovskite oxides for technological applications, and widely utilized piezoelectric materials to date. Taking into account factors such as precursor availability, ease of processing, cost-effectiveness, performance, and operating conditions, PZT is regarded as the best piezoelectric material within the perovskite family [4]. This exceptional performance is attributed to the hybridization of Pb–O bonds, the unique electronic structure of Pb (characterized by its $6s^2$ lone pair), domain wall motion, and potential disordering effects [5–9]. However, Pb alone may not be solely responsible for achieving the high piezoelectric performance. PZT is formed as a solid solution of ferroelectric $PbTiO_3$ (with a tetragonal structure and a Curie temperature, Tc, of 490°C) and antiferroelectric $PbZrO_3$ (with a rhombohedral structure and a Tc of 230°C).

CONTACT Kahoul Fares Fares.kahoul@univ-msila.dz

At room temperature, the PZT phase diagram can be broadly divided into three primary regions [10–13]. The rhombohedral (R3 m) Zr-rich region (denoted as R) is separated from the tetragonal (P4 mm) Ti-rich region (denoted as T) by a morphotropic phase boundary (MPB). Within the MPB region, the tetragonal and rhombohedral phases coexist, and PZT compositions in this region exhibit exceptional dielectric and piezoelectric properties [1,13,14]. The exact width of this zone remains unclear and varies depending on the type and concentration of dopants used [15–17]. Above the Curie temperature, the compounds adopt a paraelectric cubic phase with a Pm3 m space group.

To enhance its electrophysical properties, a dopant is introduced into the PZT-based compound. By incorporating additional components, such as a second, third, fourth, or more, the piezoelectric properties can be tuned across a wide range [13,16–21]. Compared to undoped PZT ceramics, multicomponent compounds offer several advantages, including significantly enhanced or diminished electrophysical properties.

This study centers on investigating new compositions of piezoelectric materials of the PZT type, with a particular focus on doping Sn ions at the B-sites. To achieve this, we synthesized a novel matrix of $Pb_{0.92}Ba_{0.08}(Zr_{0.49}Ti_{0.51})_{1-x}Sn_xO_3$ (abbreviated as PB–ZTS) (with x = 0, 0.02, 0.04 and 0.06) ceramics using the solid-state reaction method. The effect of SnO on the structure and electrical properties of PB–ZTS ceramics was investigated in detail. The x = 0.04 sample show high electrical parameters, such as d_{33}, Qm, Kp, ε_r and tanδ, which can meet the needs of high-power ultrasonic transducers.

2. Experimental procedure

$Pb_{0.92}Ba_{0.08}(Zr_{0.49}Ti_{0.51})_{1-x}Sn_xO_3$ (where x = 0, 0.02, 0.04 and 0.06) piezoelectric ceramics were prepared by the solid-state reaction route. The starting powders of simple oxides, PbO (99.99%), ZrO_2 (99.50%), TiO_2 (99.99%), BaO (99.90%) and SnO (99.90%) were weighed and mixed in alcohol by a magnetic stirrer for 2 h and then dried in the oven at 80°C. After milling in tungsten carbide bowls with tungsten carbide balls in alcohol medium for 8 h, the resulting slurry was dried and the powder was calcined in alumina crucible at 900°C for 2 h. The calcined powders were milled for the second time and subsequently compacted into pellets using polyvinyl alcohol (PVA) binder under a pressure of 100 MPa. The pellets were sintered at 1150°C for 4 h in a closed alumina crucibles at a heating rate of 10°C/min and natural cooling in the furnace (70°C/h), in the presence of $PbZrO_3$ powder to prevent PbO loss during the high temperature sintering. The sintered disks were coated with silver and poled in silicone oil at room temperature under 35 kV/cm for 40 min.

Room temperature powder X-ray patterns were recorded on a Philips diffractometer using CuKα radiation with a wave-length of λ = 1.54056Å in the angle range of $20° \leq 2\theta \leq 60°$ with a 10 s counting time for each step of 0.02°. The Archimedes method was used for measuring the densities of the sintered samples. Microstructure of the ceramics was examined by the scanning electron microscopy (FESEM, Quanta 250FEG, USA). The Raman spectra were recorded using a Raman spectrometer from Princeton Instruments (HORIBA HR800). Dielectric properties were obtained by measuring the temperature dependance of the capacitance and phase angle (HIOKI 3532). The piezoelectric constant (d_{33}) was measured using a quasi-static piezoelectric d_{33} meter (Model ZJ-3A, Institute of Acoustics, Chinese Academy of Science). The electromechanical coupling coefficient (Kp) and mechanical quality factor (Qm) were determined using an impedance analyzer (model HP4294A, Agilent, USA) according to the IEEE standard through resonance and anti-resonance technology.

3. Results and discussion

3.1. Structural analysis

Figure 1 presents the X-ray diffraction (XRD) patterns of PB–ZTS ceramics with different Sn contents (x). The ceramics were sintered at 1150°C for 4 h, and XRD measurements were carried out at

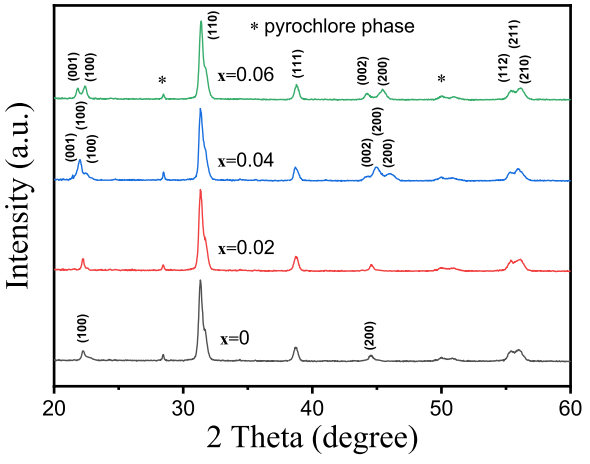

Figure 1. XRD patterns of PB–ZTS with different amounts of SnO additive, which were sintered at 1150°C for 4 h.

room temperature over a 2θ range of 20–60°. It is evident that all samples exhibit a typical perovskite structure, although a minor presence of the pyrochlore phase is also observed. The formation of this secondary phase may be attributed to lead evaporation during the sintering process [22,23]. In the perovskite structure, the (200) diffraction peak appears as a single peak in the rhombohedral (R) phase, whereas in the tetragonal (T) phase, it splits into two distinct peaks with an intensity ratio of approximately 1:2 [24–26]. The results indicate a typical coexistence of rhombohedral and tetragonal phases evidenced by the presence of $(002)_T$, $(200)_R$, and $(200)_T$ reflections at a Sn content of $x = 0.04$. When the Sn content is $x \leq 0.02$, the structure predominantly exhibits the rhombohedral phase, characterized by the $(200)_R$ peak. As the Sn content increases to $x = 0.06$, the solid solution undergoes a phase transformation, resulting in a purely tetragonal structure, as indicated by the $(002)_T$ and $(200)_T$ peaks.

3.2. Surface morphology and density analysis

Figure 2 presents SEM micrographs of PB–ZTS ceramics sintered at 1150 °C for 4 h, each with different Sn contents. The images highlight the polycrystalline structure of the samples, along with visible pores and sufficiently developed grains. Despite these features, all ceramic samples display relatively dense microstructures. Figure 2(a) displays the SEM image of the undoped PB–ZTS ceramic, which exhibits an average grain size of 552.857 nm. As the Sn doping level increases, the grain size progressively enlarges, reaching a maximum of 760.281 nm at $x = 0.04$. Compared to the undoped sample, the PB–ZTS-0.04 ceramic shows an improvement in both relative density (from 97.37% to 98.87%) and bulk density (from 7.79 g/cm^3 to 7,91 g/cm^3). These results clearly indicate that Sn addition significantly enhances the sintering performance of PB–ZTS ceramics.

This enhancement may be attributed to the fluxing effect of Sn during the ceramic sintering process, which facilitates the densification of the ceramics [27,28]. At a Sn content of 0.04, the ceramic achieves the most uniform grain distribution and the largest grain size. The observed changes in density and grain size are likely due to the substitution of Sn, which modifies the interfacial atomic structure and grain boundary energy, leading to a significant reduction in porosity [10,29]. However, when the Sn content exceeds a certain threshold, the internal lattice structure becomes disrupted, resulting in irregular grain morphology. This indicates that an optimal amount of Sn enhances the sintering process and improves the density of PB–ZTS ceramics. Such modifications in the microstructure can significantly influence the electrical properties of the ceramics [10,30].

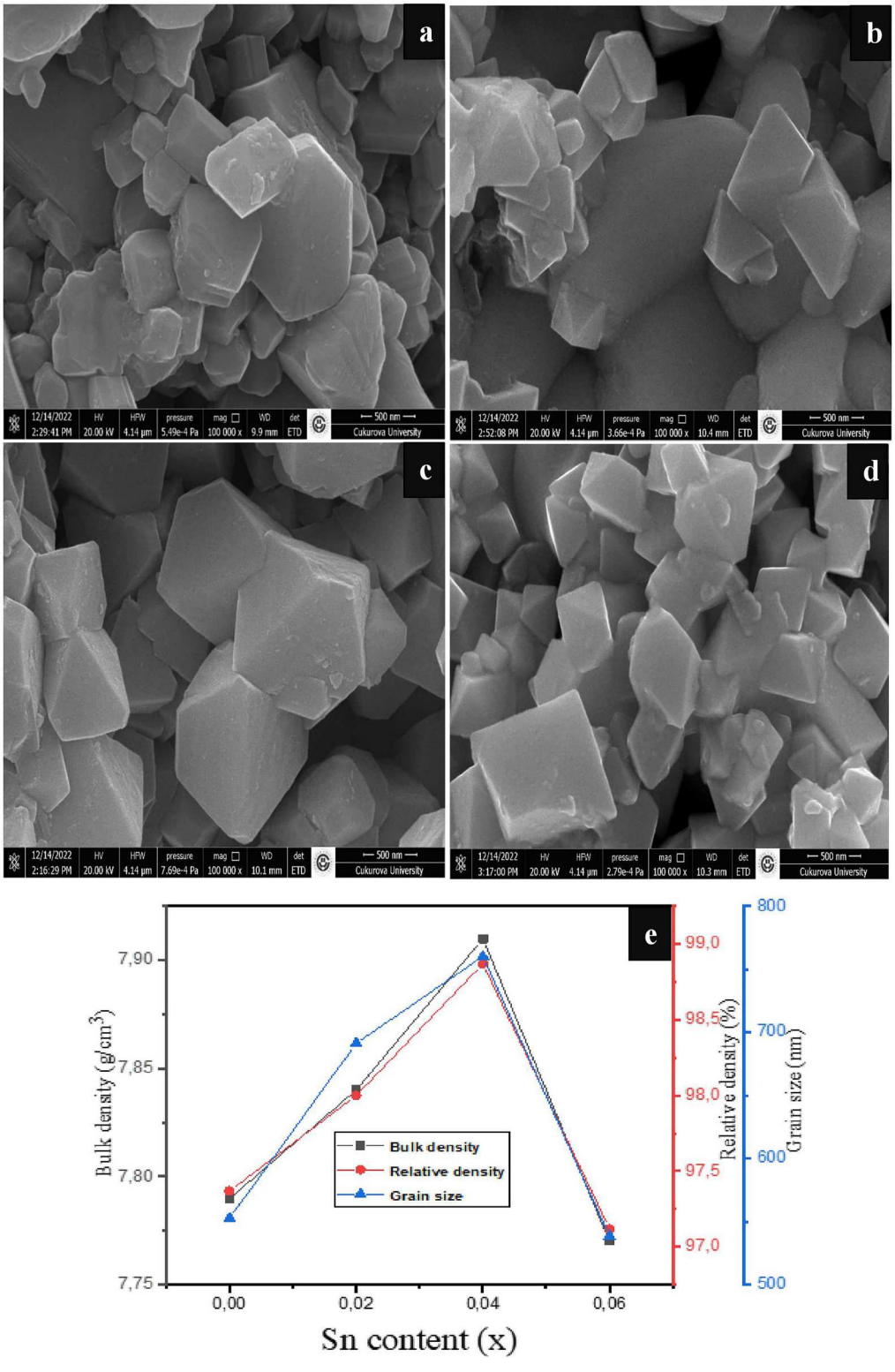

Figure 2. (a–d) SEM images for PB–ZTS ceramics sintered at 1150°C: (a) x = 0; (b) x = 0.02; (c) x = 0.04; (d) x = 0.06, (e) variation in the bulk density, relative density, and grain size, for various x values.

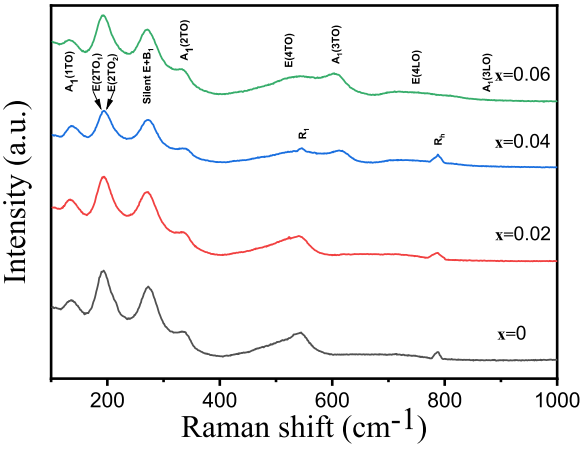

Figure 3. Raman spectra recorded in a wavenumber between 100–1000 cm^{-1} of sintered ceramics in compositions PB–ZTS with x = 0, 0.02, 0.04 and 0.06.

3.3. Raman spectroscopy analysis

Raman spectroscopy is a powerful technique for analyzing structural changes at the microscale and over short timescales. It complements XRD results by offering deeper insights into structural transformations across various compositions [31]. Figure 3 presents the room-temperature Raman spectra of PB–ZTS ceramics sintered at 1150°C, showcasing the effects of different Sn contents (x). The measurements were conducted over a wavenumber range of 100–1000 cm^{-1}. With the addition of Sn ($x \leq 0.02$), three distinct peaks emerge in the $E(2TO_2)$, R_1, and R_h modes, characteristic of the rhombohedral phase. For x values greater than 0.04, five peaks corresponding to $E(2TO_1)$, E(4TO), $A_1(3TO)$, E(4LO), and $A_1(3LO)$ become evident, indicating that Sn addition strengthens the lattice of the tetragonal phase. This enhancement promotes the phase transition from the rhombohedral to the tetragonal structure. As a result, PB–ZTS ceramics with x = 0.04 exhibit a coexistence of rhombohedral and tetragonal phases, indicating a composition close to the morphotropic phase boundary (MPB). The phase structure of Raman active modes and Raman shifts are listed in Table 1.

3.4. Dielectric and piezoelectric properties analysis

Figure 4(a–d) presents the temperature-dependent dielectric constant of PB–ZTS ceramics measured at three different frequencies (1, 10 and 20 kHz) in order to investigate the relaxor behavior of the material. The dielectric constant exhibited a peak at the Curie temperature (Tc), corresponding to the ferroelectric – paraelectric phase transition. It was observed that Tc increased

Table 1. The phase structure of Raman active modes and Raman shifts for PB–ZTS ceramics at room temperature [32,33].

Active modes	Raman shift (cm^{-1})	Phase structure
$A_1(1TO)$	140	Tetragonal or Rhombohedral
$E(2TO_1)$	188	Tetragonal
$E(2TO_2)$	196	Rhombohedral
Silien (E + B)	275	Tetragonal or Rhombohedral
$A_1(2TO)$	340	Tetragonal or Rhombohedral
E(4TO)	523	Tetragonal
R_1	583	Rhombohedral
$A_1(3TO)$	615	Tetragonal
E(4LO)	697	Tetragonal
R_h	735	Rhombohedral
$A_1(3LO)$	783	Tetragonal

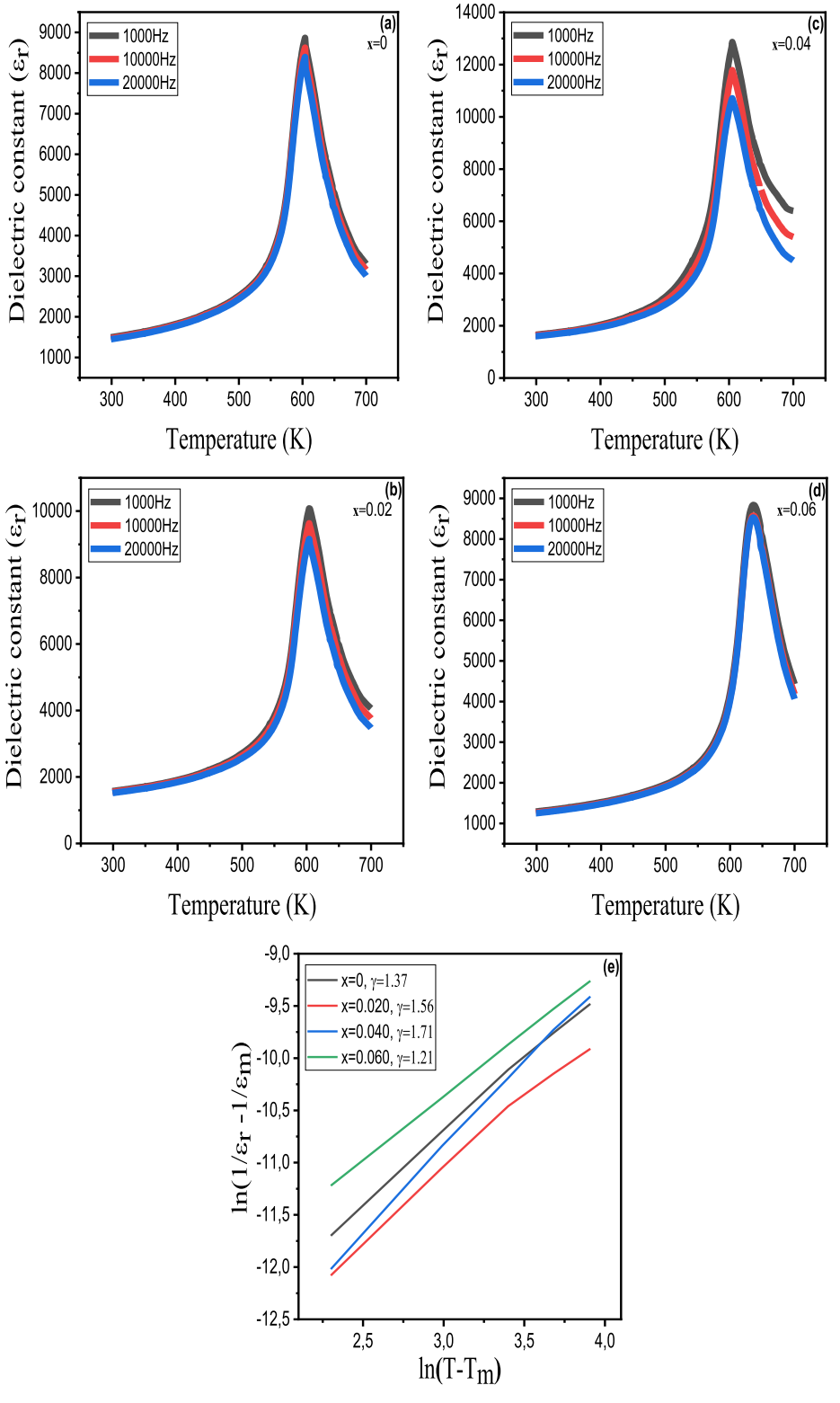

Figure 4. (a–d) Variation of dielectric constant (ε_r) with the temperature at different frequencies of ceramics for different x content, (e) $\ln(1/\varepsilon_r - 1/\varepsilon_m)$ function versus $\ln(T - T_c)$ for ceramics PB–ZTS with various x at 1 kHz.

with increasing Sn substitution. This shift in transition temperature is attributed to lattice distortion and charge imbalance defects, as Sn possesses a different ionic charge and radius compared to Ti/Zr. The dielectric constant decreased with increasing frequency, a behavior commonly observed in both dielectric and ferroelectric materials. At lower frequencies, the higher values of ε_r were attributed to the combined contribution of various polarization mechanisms, including space charge, orientation, ionic, and electronic polarization. As the frequency increases, certain polarization mechanisms become ineffective, leaving only electronic polarization active within the studied frequency range [3,34].

To gain deeper insight into the dielectric behavior of the ceramics, the modified Curie – Weiss law is applied [35,36].

$$\frac{1}{\varepsilon_r} - \frac{1}{\varepsilon_m} = \frac{(T - T_m)^\gamma}{C} \tag{1}$$

In this equation, ε_r denotes the dielectric constant at a given temperature T, while ε_m corresponds to the maximum dielectric constant observed at the transition temperature (T_m or T_c). The constant C represents the Curie constant, and γ indicates the degree of diffuseness of the phase transition, with values ranging from 1 for a typical ferroelectric to 2 for a completely diffuse phase transition [37,38].

Figure 4(e) presents the plot of $\ln(1/\varepsilon_r - 1/\varepsilon_m)$ versus $\ln(T - T_c)$ at 1 kHz for all compositions in the temperature range above T_c ($T > T_c$). The γ value progressively increases with the rising Sn concentration, reaching its peak at a content of x = 0.04. However, beyond this concentration, the γ value begins to decline. The initial increase in the γ value indicates a more pronounced diffuse phase transition with the rise in Sn content. This phenomenon is closely tied to the diffuse nature of the ferroelectric-paraelectric phase transition, attributed to the heightened γ value [39]. However, when the Sn content exceeds 0.04, a reduction in the diffuseness of the phase transition is observed, indicating the disappearance of the diffuse phase transition. This result clearly reflects the re-emergence of a typical ferroelectric behavior in this composition [40].

Figure 5(a–d) depicts the temperature-dependent dielectric loss (tan δ) of ceramics with varying Sn content, measured at frequencies of 1, 10 and 20 kHz. Notably, all ceramics exhibit a marked increase in dielectric loss tangent at elevated temperatures, which can be attributed to thermally activated space charge conduction. Broad dielectric loss peaks were also observed at higher frequencies, possibly due to the interaction between polarization mechanisms and the applied electric field. Dielectric loss peaks occurring at temperatures other than Tc may originate from dipolar defects associated with the pyrochlore phase. The magnitude of dielectric loss is likely due to the friction of rotating dipoles and an increased degree of dipole orientation [41].

Figure 6(a) illustrates the piezoelectric properties of PB–ZTS piezoceramics with varying SnO content. As depicted, both the electromechanical coupling factor (Kp) and the piezoelectric charge constant (d_{33}) follow similar variation trends as the SnO concentration increases. The sample with x = 0.04 exhibits peak values for both Kp and d_{33}, reaching 0.604 and 465 pC/N, respectively. However, the mechanical quality factor (Qm) shows an opposite trend compared to d_{33} and Kp.

Kp and d_{33} exhibit similar variation trends with the increase in average grain size. As the grain size increases with x ranging from 0 to 0.04, the clamping effect of grain boundaries on domain wall motion is significantly reduced, leading to enhanced piezoelectric properties [42]. As x increases from 0.04 to 0.06, the average grain size gradually decreases, the resulting increase in grain boundaries among smaller grains hinders domain rotation and domain wall movement, leading to a decline in electrical properties [43–45].

As illustrated in Figure 6(b), the dielectric constant (ε_r) increases, reaching a maximum value of 1654 at x = 0.04, and subsequently decreases with further increase in Sn content. Simultaneously, the tanδ values change with varying x, measured at 3.386%, 3.384%, 3.293%, and 3.584%, respectively. The fluctuations in the dielectric constant (ε_r) can be attributed to the combined effects of the ceramic phase structure and microstructural characteristics. With increasing Sn content, the

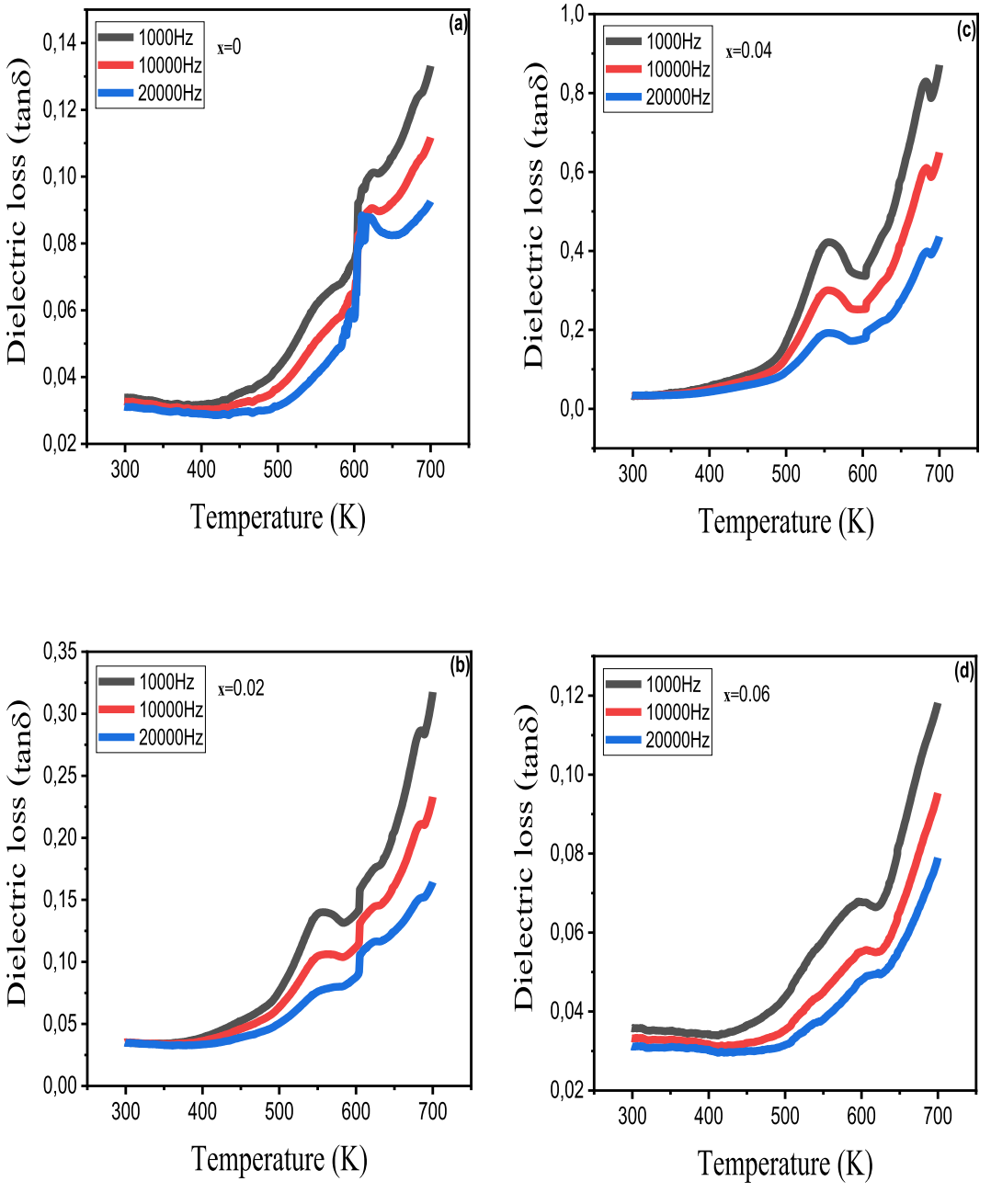

Figure 5. Temperature-frequency dependance of dielectric loss (tanδ) for PB–ZTS ceramics with x = 0-0.06.

Table 2. Details of the physical properties for PB–ZTS ceramics measured at room temperature.

Composition	Density (g/cm^3)	ε_r	tanδ	Kp	d_{33} (pC/N)	Qm
x = 0	7.79	1495	3.386%	0.562	370	872
x = 0.02	7.84	1575	3.384%	0.586	426	654
x = 0.04	7.91	1654	3.293%	0.604	465	411
x = 0.06	7.77	1292	3.584%	0.572	433	680

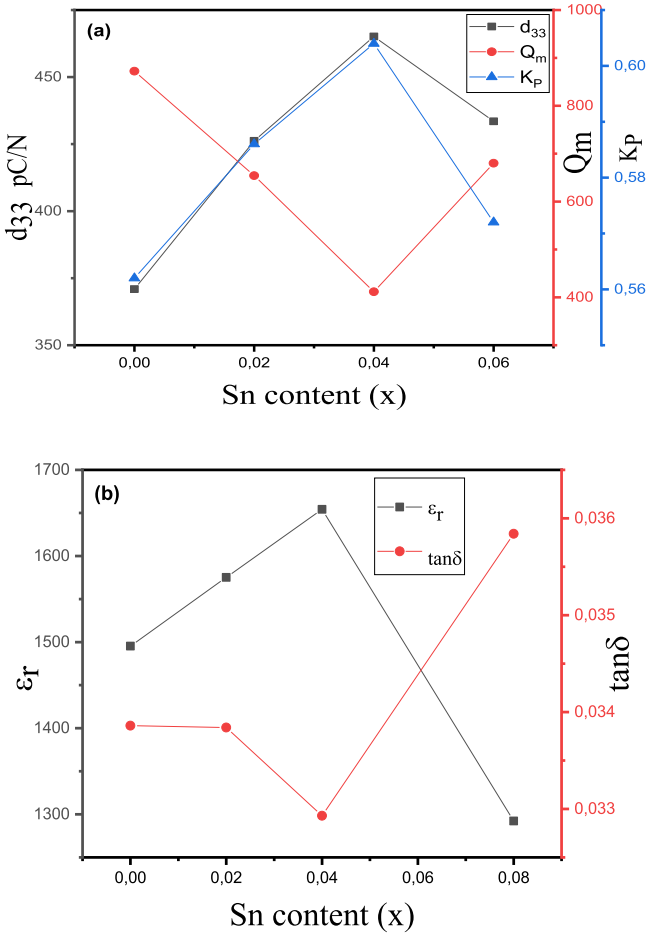

Figure 6. (a) Kp, d_{33}, and Qm as functions of SnO content measured at room temperature. (b) ε_r and tanδ as functions of SnO amount measured at 1 kHz.

composition of ceramics gradually approaches the morphotropic phase boundary (MPB). In addition, the larger grain size contributes to the increase in dielectric constant [46]. Dielectric losses in ceramics are often linked to domain wall motion, where interactions among the lattice, domain walls, and defects under an external electric field lead to energy dissipation during domain wall movement. Table 2 presents the variations in density, piezoelectric constant, and dielectric constant for each ceramic sample, providing a more comprehensive comparison of their properties.

4. Conclusions

In this study, solid solutions of $Pb_{0.92}Ba_{0.08}(Zr_{0.49}Ti_{0.51})_{1-x}Sn_xO_3$ (with x = 0, 0.02, 0.04 and 0.06) ceramics were synthesized using the conventional solid-state reaction method. The structural, microstructural and electrical properties of the ceramics were systematically investigated. An MPB region is identified in the PB–ZTS ceramics at x = 0.04, as evidenced by the XRD and Raman spectroscopy analyzes. Microscopic analysis reveals changes in the microstructure, with the highest density and optimal grain size observed at a Sn content of x = 0.04. As the x doping concentration attains 0.04, the PB–ZTS ceramics obtain the best properties, i.e. d_{33} = 465 pC/N, Kp = 0.604, Qm = 411, ε_r = 1654, tanδ = 3.293%, and bulk density = 7.91 g/cm^3. This study highlights the

potential of Sn-doped PB–ZTS ceramics for use in high-temperature piezoelectric applications, including sensors, actuators, detectors, and transformers.

Disclosure statement

No potential conflict of interest was reported by the author(s).

References

[1] Kahoul F, Benseghir S, Hamzioui L, et al. Structural, dielectric and piezoelectric characterization of BFN-modified PZT-based (MPB) ceramics. Phase Trans. 2023;96:233–245. doi:10.1080/01411594.2023.2175676

[2] Haertling GH. Ferroelectric ceramics: history and technology. J Am Ceram Soc. 1999;82:797–818. doi:10.1111/j.1151-2916.1999.tb01840.x

[3] Babu TA, Ramesh KV, Badapanda T, et al. Structural and electrical studies of excessively Sm_2O_3 substituted soft PZT nanoceramics. Ceram Int. 2021;47:31294–31303. doi:10.1016/j.ceramint.2021.08.002

[4] Jaffe B, Cook WR, Jaffe H. Piezoelectric ceramics. London-UK: Academic Press; 1971.

[5] Cohen RE. Origin of ferroelectricity in perovskite oxides. Nature. 1992;358:136–138. doi:10.1038/358136a0

[6] Szabo GS, Cohen RE, Krakauer H. First-principles study of piezoelectricity in $PbTiO_3$. Phys Rev Lett. 1998;80:4321–4324. doi:10.1103/PhysRevLett.80.4321

[7] Baettig P, Schelle CF, Sar RL, et al. Theoretical prediction of new high-performance lead-free piezoelectrics. Chem Mater. 2005;17:1376–1380. doi:10.1021/cm0480418

[8] Tanaka H, Kuroiwa Y, Takata M. Electrostatic potential of ferroelectric$PbTiO_3$: visualized electron polarization of Pb ion. Phys Rev B. 2006;74:172105–172108. doi:10.1103/PhysRevB.74.172105

[9] Kumar S, Singh DN, James AR, et al. Probing of the physical characteristics of antiferroelectric $Pb(Zr_{0.6}Ti_{0.4})O_3$ PZT (60/40) ceramics. J Mater Sci Mater Electron. 2023;34:879–884. doi:10.1007/s10854-023-10239-7

[10] Xu Y. Ferroelectric materials and their applications. New York: Elsevier; 2013.

[11] Noheda B, Cox DE. Shirane G. monoclinic ferroelectric phase in the $Pb(Zr_{1-x}Ti_x)O_3$ solid solution. Appl Phys Lett. 1999;74:2059–2061. doi:10.1063/1.123756

[12] Noheda B, Gonzalo JA, Cross LE, et al. Tetragonal-to-monoclinic phase transition in a ferroelectric perovskite: The structure of $PbZr_{0.52}Ti_{0.48}O_3$. Phys Rev B. 2000;61:8687–8695. doi:10.1103/PhysRevB.61.8687

[13] Bedoya C, Muller C, Baudour JL, et al. Sr-doped $PbZr_{1-x}Ti_xO_3$ ceramic: structural study and field-induced reorientation of ferroelectric domains. Mater Sci Eng B. 2000;75:43–52. doi:10.1016/S0921-5107(00)00383-4

[14] Soares MR, Senos AMR, Mantas PQ. Phase coexistence region and dielectric properties of PZT ceramics. J Eur Ceram Soc. 2000;20:321–334. doi:10.1016/S0955-2219(99)00170-3

[15] Bouzid A, Bourim EM, Gabbay M, et al. Pzt phase diagram determination by measurement of elastic moduli. J Eur Ceram Soc. 2005;25:3213–3221. doi:10.1016/j.jeurceramsoc.2004.07.018

[16] Mishra SK, Singhi AP, Pandey D. Thermodynamic nature of phase transitions in $Pb(Zr_xTi_{1-x})O_3$ ceramics near the morphotropic phase boundary. Philos Mag B. 1997;76:213–226. doi:10.1080/01418639708241086

[17] Bochenek D, Niemiec P. Microstructure and physical properties of the multicomponent PZT-type ceramics doped by calcium, sodium, bismuth and cadmium. Appl Phys A. 2018;124:775–781. doi:10.1007/s00339-018-2203-3

[18] Zhang RF, Zhang HP, Ma J, et al. Effect of Y and Nb co-doping on the microstructure and electrical properties of lead zirconate titanate ceramics. Solid State Ioni. 2004;166:219–223. doi:10.1016/j.ssi.2003.10.017

[19] Zachariasz R, Bochenek D. Modified PZT ceramics as a material that can be used in micromechatronics. Eur Phys J B. 2015;88:296–299. doi:10.1140/epjb/e2015-60420-y

[20] Niemiec P, Skulski R, Bochenek D, et al. Diffused AFE/RFE/PE phase transitions in (Pb0.88Ba0.1La0.02)(Zr0.6Sn0.4−xTix)0.995O3 ceramics obtained from oxides and carbonates. Phase Trans. 2013;86:267–274. doi:10.1080/01411594.2012.715298

[21] Zachariasz R, Ilczuk J, Bochenek D. Influence of the technology conditions on the mechanical and dielectric properties of the PZT-base piezoceramic transducers. Solid State Phenom. 2003;89:303–308. doi:10.4028/www.scientific.net/SSP.89.303

[22] Fan H, Kim HE, Zhu JG. Perovskite stabilization and electromechanical properties of polycrystalline lead zinc niobate–lead zirconate titanate. J Appl Phys. 2002;91:317–322. doi:10.1063/1.1421036

[23] Du J, Yang C, Li Y, et al. Microstructural, dielectric, piezoelectric and ferroelectric properties of xPZN–PZT ternary ceramics. J Mater Sci Mater Electron. 2023;34:780–789. doi:10.1007/s10854-023-10152-z

[24] Qiao H, He C, Wang Z, et al. Improved electrical properties of $BaTiO_3$ modified $BiScO_3$–$PbTiO_3$ ceramics with high curie temperature. Ceram Int. 2017;43:11463–11468. doi:10.1016/j.ceramint.2017.06.021

[25] Wang P, Guo Q, Li F, et al. $Pb(In_{1/2}Nb_{1/2})O_3$–$PbZrO_3$–$PbTiO_3$ ternary ceramics with temperature-insensitive and superior piezoelectric property. J Eur Ceram Soc. 2022;42:3848–3856. doi:10.1016/j.jeurceramsoc.2022.03.016

[26] Lu X, Hao Y, Yang T. Achieving superior energy harvesting performance in Sr-doped (Pb, La, Sb)(Zr. Ti(O3). ceramics based on optimization of FOM. J Mater Sci Mater Electron. 2023;34:653–661. doi:10.1007/s10854-023-10014-8

[27] Kanai H, Furukawa O, Abe H, et al. Dielectric properties of $(Pb_{1-x}X_x)$ $(Zr_{0.7}Ti_{0.3})O_3$ (X = Ca, Sr. Ba) ceramics. J Am Ceram Soc. 1994;77:2620–2624. doi:10.1111/j.1151-2916.1994.tb04652.x

[28] Kozielski L, Adamczyk M, Erhart J, et al. Application testing of Sr doping effect pf PZT ceramics on the piezoelectric transformer gain and efficiency proposed for MEMS actuators driving. J Electroceram. 2012;29:133–138. doi:10.1007/s10832-012-9746-z

[29] Ye S, Fuh J, Lu L. Effects of Ca substitution on structure, piezoelectric properties, and relaxor behavior of lead-free $Ba(Ti_{0.9}Zr_{0.1})O_3$ piezoelectric ceramics. J Alloys Compd. 2012;541:396–402. doi:10.1016/j.jallcom.2012.06.084

[30] Qian H, Yan Y, Luo F, et al. Simultaneously improving piezoelectricity and temperature stability of $0.05Pb(Yb_{1/2}Nb_{1/2})O_3$ $0.95Pb(Hf_{0.45}Ti_{0.55})O_3$ ceramics by Sr^{2+} substitution. J Mater Sci Mater Electron. 2023;34:606–621. doi:10.1007/s10854-023-10019-3

[31] Benseghir S, Kahoul F, Hamzioui L, et al. Phase transition, microstructure and electrical properties of $Pb_{1-x}Y_{x/2}Bi_{x/2}[(Zr_{0.53}Ti_{0.47})_{0.92}$–$(Mn_{1/3}Sb_{2/3})_{0.08}]O_3$ piezoelectric ceramics. Ferroelectrics. 2021;584:198–211. doi:10.1080/00150193.2021.1984780

[32] Djoudi Y, Kahoul F, Hamzioui L, et al. Influence of YTS addition on structural and electrical properties of PZT-based ceramics. Proces Appl Ceram. 2021;15:279–287. doi:10.2298/PAC2103279D

[33] Kahoul F, Hamzioui L, Guemache A, et al. Study of dielectric and piezoelectric properties of (1-x)PZT-xSFN ceramics prepared by conventional solid state reaction method. J Chem Soc Pak. 2020;42:634–638.

[34] Kour P, Pradhan S, Kumar P, et al. Effect of Nd doping on dielectric and impedance properties of PZT nanoceramics. J Electron Mater. 2018;47:2861–2870. doi:10.1007/s11664-018-6151-7

[35] Chen H, Xing J, Xi J, et al. Origin of high piezoelectricity in low- temperature sintering PZT-based relaxor ferroelectric ceramics. J Alloys Compd. 2021;860:157930–157937. doi:10.1016/j.jallcom.2020.157930

[36] Li X, Ma J, Chen K, et al. Design and investigate the electrical properties of $Pb(Mg_{0.2}Zn_{0.2}Nb_{0.2}Ta_{0.2}W_{0.2})O_3$–$PbTiO_3$ high-entropy ferroelectric ceramics. Ceram Int. 2022;48:12848–12855. doi:10.1016/j.ceramint.2022.01.156

[37] Du J, Qiu L, Xiao X, et al. High piezoelectricity in PFN–PNN–PZT quaternary ceramics achieved via composition optimization near morphotropic phase boundary. Ceram Int. 2022;48:30891–30899. doi:10.1016/j.ceramint.2022.07.043

[38] Sun Z, Li L, Zheng H, et al. Dielectric properties and diffuse phase transition behavior of CuO-doped lead-free $Ba(Zr_xTi_{1-x})O_3$ ceramics. Ceram Int. 2016;42:12246–12252. doi:10.1016/j.ceramint.2016.04.170

[39] Quang DA, Vuong LD. Enhanced piezoelectric properties of Fe_2O_3 and Li_2CO_3 co-doped $Pb[(Zr_{0.48}Ti_{0.52})_{0.8}(Zn_{1/3}Nb_{2/3})_{0.125}(Mn_{1/3}Nb_{2/3})_{0.075}]O_3$ ceramics for ultrasound transducer applications. J Sci Adva Mate Devic. 2022;7:100436–100447.

[40] Ranjan R, Kumar R, Behera B, et al. Effect of Sm on structural, dielectric and conductivity properties of PZT ceramics. Mater Chem Phys. 2009;115:473–477. doi:10.1016/j.matchemphys.2009.01.017

[41] Goel P, Yadav KL, James AR. Double doping effect on the structural and dielectric properties of PZT ceramics. J Phys D Appl Phys. 2004;37:3174–3179. doi:10.1088/0022-3727/37/22/019

[42] Hou YD, Chang LM, Zhu MK, et al. Effect of Li_2CO_3 addition on the dielectric and piezoelectric responses in the low-temperature sintered 0.5PZN–0.5PZT systems. J Appl Phys. 2007;102:84507–84513. doi:10.1063/1.2800264

[43] Okazaki K, Sakata K. Space charge polarization and aging of barium titanate ceramics. Electrotech J Jpn. 1962;7:13–18.

[44] Schultheib J, Checchia S, Ursic H, et al. Domain wall-grain boundary interactions in polycrystalline $Pb(Zr_{0.7}Ti_{0.3})O_3$ piezoceramics. J Eur Ceram Soc. 2020;40:3965–3973. doi:10.1016/j.jeurceramsoc.2020.03.054

[45] Li X, Cheng Y, Wang F, et al. Enhancement of energy storage and hardness of $(Na_{0.5}Bi_{0.5})_{0.7}Sr_{0.3}TiO_3$-based relaxor ferroelectrics via introducing $Ba(Mg_{1/3}Nb_{2/3})O_3$. Chem Eng J. 2022;431:133441–133447. doi:10.1016/j.cej.2021.133441

[46] Yang ZP, Li H, Zong XM, et al. Structure and electrical properties of PZT–PMS–PZN piezoelectric ceramics. J Eur Ceram Soc. 2006;26:3197–3202. doi:10.1016/j.jeurceramsoc.2005.08.005